nature physics

Article

https://doi.org/10.1038/s41567-025-02912-x

Interplay between light and heavy electron bands in magic-angle twisted bilayer graphene

Received: 18 February 2024

Accepted: 8 April 2025

Published online: 22 May 2025

Check for updates

Rafael Luque Merino[1,2,3], Dumitru Călugăru[4,5], Haoyu Hu[6], Jaime Díez-Mérida[1,2,3], Andrés Díez-Carlón[1,2,3], Takashi Taniguchi[7], Kenji Watanabe[8], Paul Seifert[1,9], B. Andrei Bernevig[4,6,10] & Dmitri K. Efetov[2,3]

Recent studies have suggested that the strongly correlated flat bands of magic-angle twisted bilayer graphene may host coexisting light and heavy carriers. Although transport and spectroscopic measurements have hinted at this behaviour, distinct signatures of incoherent heavy carriers have not been reported. Here we provide evidence of this by performing thermoelectric transport measurements of magic-angle twisted bilayer graphene using the photo-thermoelectric effect in gate-defined p–n junctions. At low temperatures, we observe sign-preserving, filling-dependent oscillations of the Seebeck coefficient at non-zero integer fillings of the moiré superlattice. This suggests the preponderance of one carrier type even when the Fermi level is tuned through the charge neutrality point of the correlated states. At higher temperatures, the thermoelectric response provides evidence of strong electron correlations in the unordered, normal state. Our observations are explained by the interplay between light, long-lived electron states and heavy, short-lived hole excitations near the Fermi level of the symmetry-broken ground states. These findings are in qualitative agreement with the topological heavy fermion model.

The flat bands of magic-angle twisted bilayer graphene[1] (MATBG) offer a rich playground for condensed matter physics, as they host both strong electronic interactions and non-trivial topology[2]. A variety of symmetry-breaking ground states emerge at non-zero integer fillings of the moiré unit cell ν, where $\nu = 4n/n_s$ and n_s is the carrier density in a fully occupied moiré band. The contrasting properties of its ground states (which include superconductivity[3–5], Mott-like physics[4,6] and topological states[7–10]) suggest the coexistence of itinerant and localized electrons within the flat bands. In addition, the sawtooth-like evolution of the electronic entropy[11–15] around integer ν, as well as the presence of Landau fans that only disperse away from the charge neutrality point (CNP)[3–6], point to a distinct asymmetry of the charge ± 1 excitations of the symmetry-broken ground states.

Thermoelectric transport, parameterized by the Seebeck coefficient (S), constitutes an accurate probe of Fermi surface properties of condensed matter systems. In particular, S is highly sensitive to the

[1]ICFO – Institut de Ciencies Fotoniques, The Barcelona Institute of Science and Technology, Castelldefels, Spain. [2]Fakultät für Physik, Ludwig-Maximilians-Universität, Munich, Germany. [3]Munich Center for Quantum Science and Technology (MCQST), Munich, Germany. [4]Department of Physics, Princeton University, Princeton, NJ, USA. [5]Rudolf Peierls Centre for Theoretical Physics, University of Oxford, Oxford, UK. [6]Donostia International Physics Center (DIPC), San Sebastián, Spain. [7]International Center for Materials Nanoarchitectonics, National Institute for Materials Science, Tsukuba, Japan. [8]Research Center for Functional Materials, National Institute for Materials Science, Tsukuba, Japan. [9]Institute of Physics and SENS Research Centre, University of the Bundeswehr Munich (UniBw M), Neubiberg, Germany. [10]IKERBASQUE, Basque Foundation for Science, Bilbao, Spain. e-mail: dmitri.efetov@lmu.de

https://doi.org/10.1038/s41567-025-02912-x

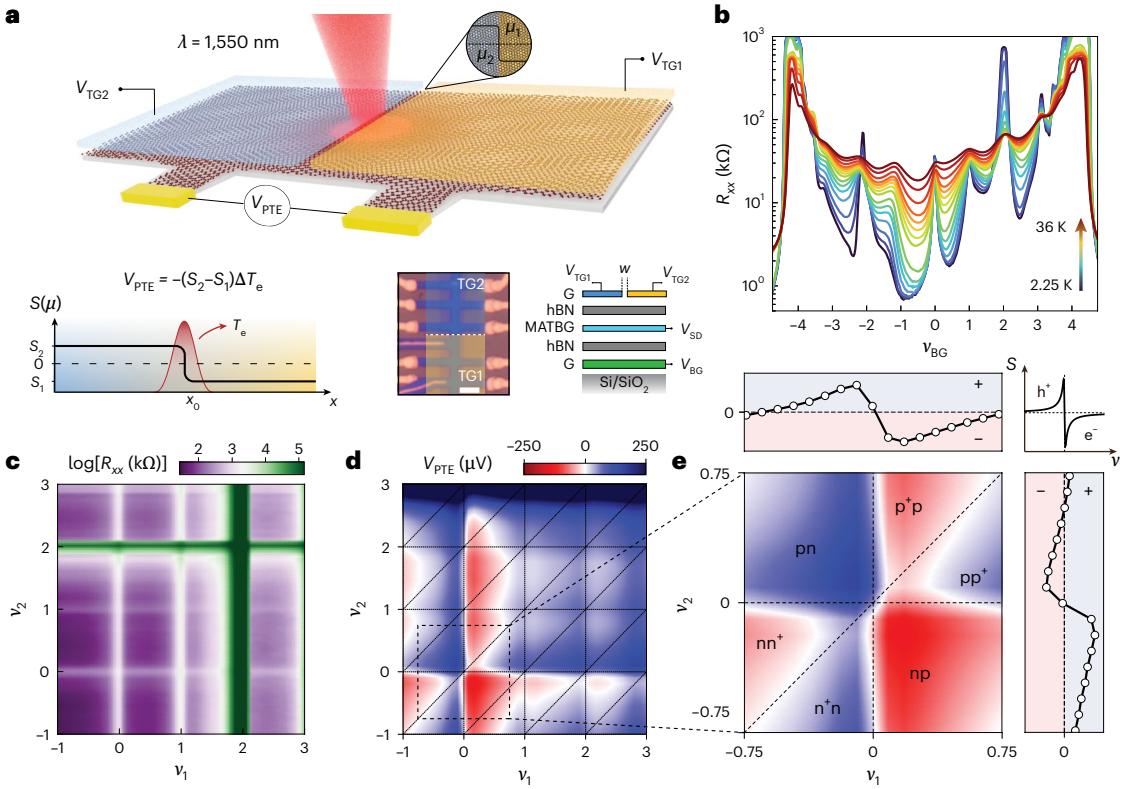

Fig. 1 | PTE effect in a gate-defined MATBG p–n junction. a, A local thermal gradient is created at the interface of a MATBG p–n junction using a focused laser beam. The gate-defined step in μ enables the generation of V_{PTE} across the junction. V_{TG1} and V_{TG2}, top-gate voltages; hBN, hexagonal boron nitride. Insets: origin of V_{PTE} (left; x_0 denotes the junction position), an optical micrograph of the sample (middle) and a schematic cross-section of the heterostructure (right; V_{BG}, back-gate voltage; V_{SD}, source–drain voltage for the transport measurements; w, junction width; G, few-layer graphite used as top and back gates.). **b**, Temperature-dependent four-terminal resistance of Device 1 ($\theta = 1.14°$) before splitting the top gate at 2.25, 2.8, 3.6, 5, 6.5, 5, 8, 10, 12, 14, 16, 18, 20, 24, 30 and 36 K. **c**, Dual-gate map of R_{xx} of Device 1 at $T_L = 35$ mK. Correlated states for each side of the junction appear at integer values of ν_1 and ν_2. **d**, V_{PTE} response in the electron-doped flat bands of Device 1 at $T_L = 10$ K. Oscillations emerge around each integer filling. **e**, V_{PTE} response near the CNP shows a characteristic six-fold symmetry, which confirms the thermoelectric origin of the response. Dashed lines in **d** and **e** are visual guides. Insets: linecuts of the dual gate map along the horizontal and vertical dashed lines, where one of the top gates is kept at neutrality. All gate voltage dependences are plotted as a function of the filling of the moiré bands. This conversion is calculated using the carrier density at full filling and the gate capacitances, which are both extracted from magneto-transport data.

band dispersion and the scattering mechanisms near the Fermi level E_F. Generally, the sign and magnitude of S contain information about the charge of the majority carriers and their effective masses, as described by the semiclassical Mott relation[16] (SMR) $S_{Mott} \propto -T\frac{\partial}{\partial\mu}\ln\sigma(\mu)$, where T, μ and σ are the temperature, chemical potential and conductivity, respectively. In strongly correlated systems, such as cuprate superconductors[17–19], heavy fermion compounds[20,21] or narrow gap semiconductors[22–25], deviations from the SMR can arise due to the coexistence of contrasting electronic orbitals[21,25], reconstructing Fermi surfaces[17,18] and the finite lifetimes of incoherent electron excitations[19,24].

The thermoelectricity in the MATBG flat bands has been shown to violate the SMR[26–28]. Previous works reported no sign changes in S at integer fillings, where $\sigma(\mu)$ peaks, and observed a nonlinear temperature dependence where S does not extrapolate to zero in the limit of $T \to 0$. This non-semiclassical thermoelectric response was attributed to electron–hole (e–h) asymmetry in the density of states of the flat bands. However, these studies used MATBG samples that lacked well-developed, symmetry-broken correlated states, which are predicted to be e–h asymmetric[29–33]. These findings were modelled using weakly interacting frameworks based on the SMR. Crucially, the SMR is not applicable to the MATBG flat bands, because it assumes rigid band filling. In addition, it neglects effects such as band-dependent scattering rates, which can substantially alter thermoelectric transport[34].

In this Article, we explore the low-temperature thermoelectricity of the MATBG flat bands through optical excitation of gate-defined p–n junctions. We find strong evidence of photo-thermoelectric (PTE) voltage generation driven by the Seebeck effect in the MATBG flat bands. The PTE response develops oscillations at each integer filling, which arise from the formation of symmetry-broken correlated states. The thermoelectricity remains electron-like for positive fillings of the flat bands, despite interaction-induced reconstructions of the charge-one excitation bands and the opening of gaps around integer fillings. This observation points to a scenario in which electrons with long transport lifetimes dominate the thermoelectric transport over incoherent hole-like excitations. We provide a natural interpretation via the topological heavy fermion (THF) mapping of MATBG[35,36], where the contrasting properties of light and heavy electrons[37] inherently account for the observed response. We also study the high-temperature thermoelectricity of the flat bands, finding signatures of the persistent influence of strong electron correlations, even in the absence of symmetry-breaking ordered states.

We probed the low-temperature thermoelectric transport of the flat bands using laser excitation (at wavelength $\lambda = 1{,}550$ nm) to locally heat up a MATBG p–n junction, as sketched in Fig. 1a. We focused on two high-quality MATBG samples (with twist angles $\theta = 1.14°$ and $\theta = 1.06°$) that exhibit well-developed correlated resistive states at non-zero ν (Fig. 1b), as well as superconducting phases (Supplementary Information). We note that both devices feature large activation

https://doi.org/10.1038/s41567-025-02912-x

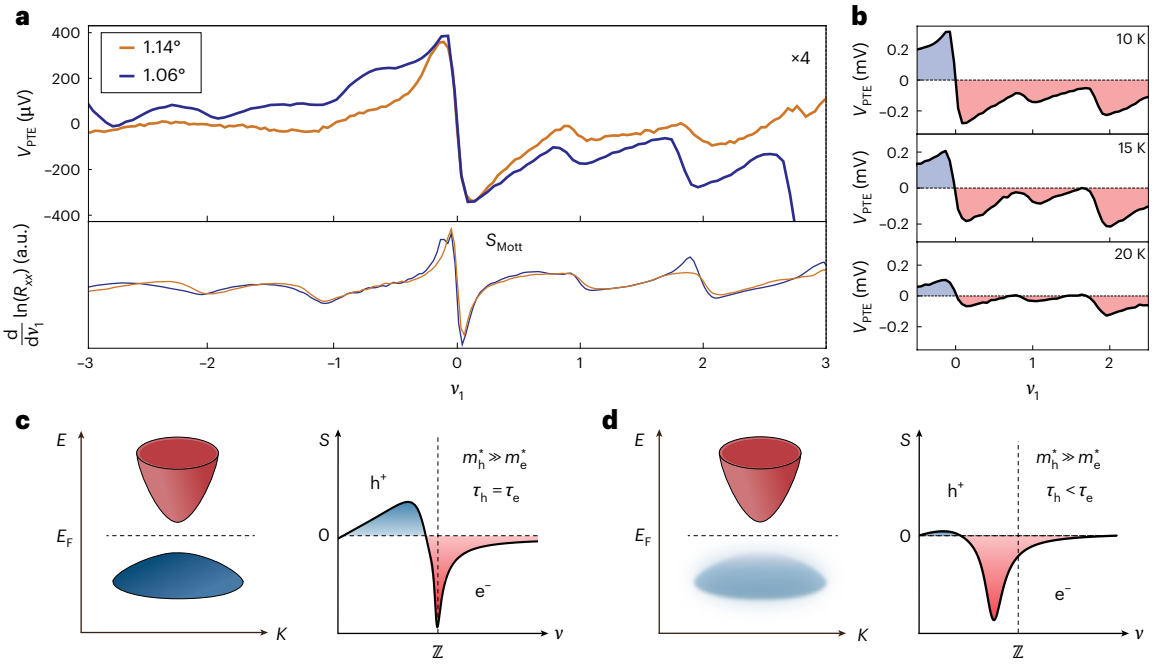

Fig. 2 | Sign-preserving thermoelectric responses in the flat bands at low temperatures. a, PTE response across the flat bands at $T_L = 10$ K under low-power excitation for Device 1 ($\theta = 1.14°$) and Device 2 ($\theta = 1.06°$). In this measurement, $S_2 = 0$. Bottom: expectation from the semiclassical Mott formula, where $S_{Mott} \propto \frac{d}{d\nu_1}\ln(R_{xx})$. The response of Device 1 has been scaled by a factor of 4. **b**, Temperature-dependent thermoelectric response for Device 2 at 10 K (top), 15 K (middle) and 20 K (bottom). As T_L increases, the response evolves towards conventional sign-changing thermoelectricity at integer fillings. **c**, Left: two-band model for a generic symmetry-broken ground state at $\nu = \mathbb{Z}$ with large effective mass asymmetry ($m_h^* \gg m_e^*$) and equal scattering lifetimes $\tau_h = \tau_e$. Right: computed Seebeck coefficient in the scenario of extreme mass asymmetry ($m_h^* = 150\, m_e^*$), exhibiting slight e–h asymmetry but preserving the sign change near $\nu = \mathbb{Z}$. **d**, Left: band structure for $\nu = \mathbb{Z}$ in a two-band, light–heavy scenario where the two bands feature distinct scattering rates (carrier lifetimes). The hole band has a shorter carrier lifetime, illustrated by spectral broadening of the states ($\tau \propto 1/\Delta E$). Right: computed Seebeck coefficient in the light–heavy scenario with $m_h^* = 150\, m_e^*$, $\tau_e = 6\tau_h$. The lifetime asymmetry drastically modifies the Seebeck coefficient, which becomes fully negative across the integer filling.

gaps at half-filling ($\Delta_{+2} \approx 1.9$ meV), demonstrating the presence of strong electronic interactions. A gate-defined p–n junction was created by splitting the top graphite gate, allowing independent control of the carrier concentration on each side. The junction was defined in a section of the Hall bar device with a homogeneous twist angle near 1.1°. Figure 1c depicts the dual top-gate map of the junction's longitudinal resistance (R_{xx}), where both sides of the junction feature pronounced correlated states that can be addressed independently.

The continuous-wave excitation induces a local increase in the electronic temperature ΔT_e centred at the junction's interface. Using the split top gates, we established a chemical potential difference $\Delta\mu$ (and so a Seebeck coefficient difference ΔS) across the junction. The gate-dependent response around the CNP exhibits multiple sign changes in a characteristic six-fold pattern (Fig. 1e), as reported previously for single-layer graphene[38]. This pattern reflects the antisymmetric gate-dependence of S in e–h-symmetric semimetals and semiconductors. Here, the sign of the net PTE voltage (V_{PTE}) does not depend only on the polarity of the junction (p–n or n–p), as in the photovoltaic effect, but is instead determined by the Seebeck coefficient on each side of the junction (the sign of the response is reversed between pp+ and p$^+$p). This clearly establishes the PTE effect as the origin of the optoelectronic response[38,39]. In the Supplementary Information we discuss and rule out contributions from other potential mechanisms of voltage generation.

We consistently found six-fold symmetric patterns around the CNP across multiple samples and various experimental conditions (Supplementary Fig. 18). This results in a net PTE voltage given by $V_{PTE} = -(S_2 - S_1)\Delta T_e$, with $S_i(\mu_i)$ the Seebeck coefficient of each side of the junction[38–41] (see the lower left sketch in Fig. 1a). We note that the PTE effect confers multiple advantages for the study of thermoelectric transport, including spatial control of the ΔT_e profile and efficient carrier heating in graphene-like systems[42,43].

The PTE response indicates graphene-like, hot carrier dynamics in MATBG for above-gap excitation. Here the absorbed photon energy is efficiently converted into an increased temperature $T_e + \Delta T_e$ of the carrier distribution at E_F, while the phonon degrees of freedom stay in equilibrium at lattice temperature T_L (ref. 44). As the MATBG flat bands lie near E_F, thermoelectric transport of the hot carriers serves as a powerful tool to probe the low-energy electronic spectrum of MATBG. This picture is consistent with existing studies of light–matter interactions in MATBG in this wavelength range[45,46], which we discuss in Supplementary Section V. In the following, we leverage the PTE response of the p–n junction to investigate the low-energy electronic spectrum of the strongly interacting flat bands.

We explored the thermoelectric response of the p–n junction, focusing on the conduction flat band ($\nu > 0$), which exhibits stronger correlated states in transport. In Fig. 1d, the dual gate map of $V_{PTE}(\nu_1, \nu_2)$ reveals multiple sign changes that appear at integer ν_i for each side of the junction. These features coincide with the correlated states in the dual-gate R_{xx} map, indicating that V_{PTE} captures the interaction-driven instabilities of the MATBG flat bands[11–13]. To study these oscillations in more detail, we simplified the measurement scheme by fixing one side of the junction at the CNP, so that $S_2 = S_{CNP} = 0$. The PTE response then reads $V_{PTE} = -(S_2 - S_1)\Delta T_e = S_1 \Delta T_e$, and can be directly linked to S_1. We focused on this side of the junction because $R_{xx}(\nu_1)$ exhibits larger resistive peaks than $R_{xx}(\nu_2)$. This measurement scheme mimics the configuration used in Joule heating approaches, which feature a homogeneous S and an asymmetric ΔT_e. We restricted ourselves to the linear heating regime ($\Delta T_e < T_e = T_L$) by using low excitation powers. We estimated ΔT_e using a steady-state, two-temperature

https://doi.org/10.1038/s41567-025-02912-x

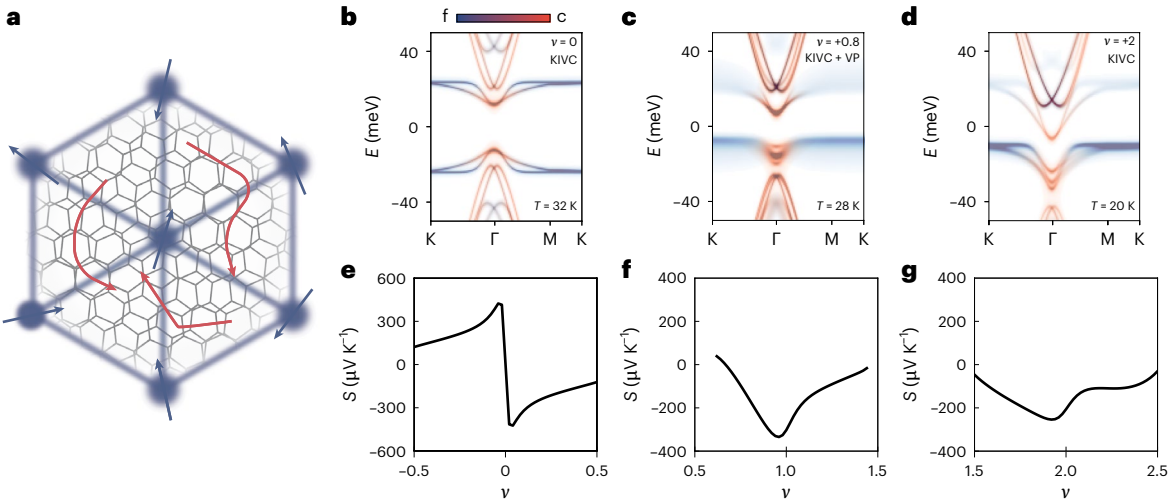

Fig. 3 | Seebeck coefficient of the symmetry-broken ground states in the THF model. a, Illustration of the coexisting electronic species in the THF mapping of MATBG. The c electrons (red) are itinerant and weakly interacting, while the f electrons (blue) are highly localized in the moiré scale and incoherent due to strong electronic interactions. **b**–**d**, THF band structures for the KIVC symmetry-broken correlated ground states around $\nu = 0$ (**b**), 0.8 (**c**) and 2 (**d**). The colour coding of the bands indicates their light or heavy character. The band structure in **c** is shown away from $\nu = 1$ to highlight the spectrally broadened f states. **e**, Seebeck coefficient for the KIVC state in **b** at $\nu = 0$. **f**, Seebeck coefficient for the KIVC + valley-polarized (VP) state in **c** in the vicinity of $\nu = 1$. **g**, Seebeck coefficient for the KIVC state in **d** in the vicinity of $\nu = 2$. At positive, non-zero integer fillings, the hole bands are formed by incoherent f electron excitations and give rise to a sign-preserving, oscillating Seebeck coefficient. The Seebeck coefficients in **e**–**g** are computed for $T \approx 0.65 T_{\text{order}}$.

model that includes the experimentally determined thermal relaxation time of the devices (Supplementary Section IV).

The low-temperature, gate-dependent thermoelectric response $V_{\text{PTE}}(\nu_1)$ of both devices is shown in Fig. 2a. The evolution of V_{PTE} across the CNP is conventional, exhibiting an antisymmetric, sign-changing doping dependence, where holes result in a positive S and electrons in a negative S. Following electron doping of the flat bands, we observed oscillatory features of the thermoelectric response around each integer ν_1. These oscillations can be attributed to the formation of symmetry-breaking ground states[36]. Strikingly, V_{PTE} remains electron-like (negative) at $\nu_1 = 1,2$, despite the prominent gap-like oscillations. This sign-preserving thermoelectric response contrasts with the SMR expectation, where the Seebeck coefficient S_{Mott} should cross zero when the carrier type changes across gaps or at extrema of the density of states. The negative sign of V_{PTE} indicates reduced hole contributions to thermoelectricity, highlighting the pronounced e–h asymmetry of the charge excitations of the symmetry-broken ground states.

In the electron-doped flat bands ($\nu_1 > 0$), the magnitude of V_{PTE} decreases for increasing T_{L}, as shown in Fig. 2b. Within the studied temperature range, the Seebeck-driven response did not extrapolate to zero as $T_{\text{L}} \to 0$. This observation, previously reported in strongly correlated systems[17–20,23], underscores the key role of non-semiclassical correlation effects in thermoelectric transport in the MATBG flat bands. The hole peak in the V_{PTE} oscillations around $\nu_1 = 1,2$ recovers its positive sign at $T_{\text{L}} = 20$ K, in agreement with the computed ordering temperatures of the symmetry-broken phases in MATBG[47].

In Fig. 2c,d we illustrate different scenarios for e–h asymmetry in the electron-doped correlated states. Following the interaction-induced reconstruction of the Fermi surface, the MATBG flat bands are known to support symmetry-broken ground states at integer fillings $\nu = \mathbb{Z}$. The charge-one excitations above these ground states can be phenomenologically modelled by two quadratically dispersing bands around E_{F} (Fig. 2c)[30,31]. We first considered strong mass asymmetry of the bands as the potential origin of the sign-preserving thermoelectric response. In this scenario, the hole band has larger effective mass $m_{\text{h}}^* \gg m_{\text{e}}^*$, but all carriers share a common carrier lifetime τ. Within a two-band model[36], we computed S under conditions of extreme mass asymmetry ($m_{\text{h}}^* = 150 m_{\text{e}}^*$). The Seebeck coefficient (Fig. 2c, right) exhibits reduced hole-like contributions but still features a zero crossing across the gap. The persistence of the sign change suggests that asymmetry in the dispersion of the electron and hole bands is insufficient to explain the observed behaviour. Other factors beyond the band dispersion, such as the carrier scattering rate in the flat bands, must also be considered.

Realistic modelling of the transport properties of the correlated states of MATBG must account for the energy (or band) dependence of the carrier lifetime $\tau = \tau(E)$. Next, we included a band-dependent carrier lifetime in the two-band model (Fig. 2d). By considering $\tau_{\text{e}} = 6\tau_{\text{h}}$ and maintaining the mass asymmetry ratio at $m_{\text{h}}^* = 150 m_{\text{e}}^*$, we replicated the electron-like oscillations of the Seebeck coefficient (Fig. 2d). In this scenario, hole-like transport is suppressed through the combined effects of the increased scattering rate, which reduces τ_{h}, and the lower group velocity $v_{\text{g}}(E)$ of the hole band. Notably, S exhibits electron-like characteristics even for sizable hole doping of the symmetry-broken ground state at $\nu = \mathbb{Z} - \delta$. This observation strongly suggests that the energy dependence of $\tau(E)$, set by the scattering processes, profoundly influences the thermoelectric transport of such general correlated ground states. Similar effects have been reported in other strongly correlated systems[23,24], including heavy fermion compounds[21,48]. In localized heavy bands, e–e interactions can induce large scattering rates that result in shorter transport lifetimes and diminished transport contributions.

While this minimal model already contains the main features needed to explain the anomalous PTE response—the mass and lifetime asymmetry—we further compared our results with the recently developed THF mapping of MATBG[35]. In the THF model, the flat bands result from the hybridization between strongly correlated, highly localized heavy f electrons and highly dispersive, itinerant light c electrons (Fig. 3a). The topology is then carried by the light electrons, while the flatness of the bands is a direct consequence of the localized nature of the heavy electrons. This model therefore naturally accommodates coexisting electronic species with contrasting transport coefficients. The c electrons form coherent excitations that dominate the transport properties, whereas the incoherent excitations formed by f electrons do not contribute directly to transport. Indirectly, however, the strong

https://doi.org/10.1038/s41567-025-02912-x

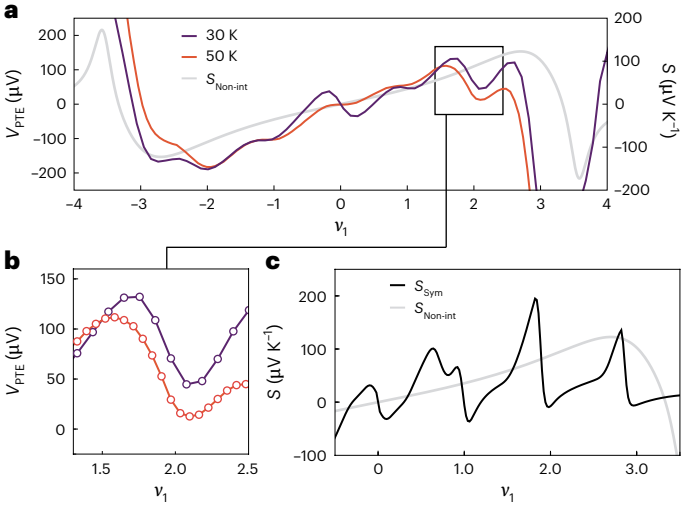

Fig. 4 | Thermoelectric response in the high-temperature, symmetric state of MATBG. a, PTE response in Device 2 ($\theta = 1.06°$) at $T_L = 30$ K (purple) and 50 K (red). The grey trace shows the expectation from the non-interacting limit of the THF model ($S_{Non\text{-}int}$) for $T_L = 15$ K, $\tau_e/\tau_h = 4$. **b**, Zoom-in of the high-temperature oscillations of the thermoelectric response near $\nu = 2$. **c**, S_{Sym} of the THF model at $T_L = 15$ K. The grey trace depicts $S_{Non\text{-}int}$ at the same temperature.

interactions between localized f electrons may impact electronic transport by breaking the global symmetries of MATBG and inducing gaps in the dispersion of the c electrons. In what follows, we provide a microscopic model for the low-temperature thermoelectricity of MATBG by considering the symmetry-broken phases of the THF model. The latter have been shown to persist for finite doping and relatively low temperatures[47].

Using self-consistent second-order perturbation theory[36], we computed the interacting energy bands and corresponding Seebeck coefficients for the correlated insulating ground states of MATBG at twist angle $\theta = 1.06°$. All computed band structures and S correspond to temperatures $T \approx 0.6\text{–}0.7 T_{order}$, where T_{order} denotes the self-consistently determined ordering temperature of each ground state. The low-temperature band structures of the Kramers intervalley coherent (KIVC)[35,49], or KIVC + valley-polarized, ground states near integer fillings $\nu = 0,1,2$ are shown in Fig. 3b–d. The colour coding denotes the light (c) or heavy (f) character of the bands (Fig. 3a). The coherent (incoherent) excitations appear as sharp (blurred) energy states, associated with long (short) transport lifetimes. Generally, the *c* electron states form the bands near Γ, while f states appear away from the Brillouin zone centre.

The essential properties of the THF band structures discussed here do not depend on the exact choice of the symmetry-broken ground state[36]. Other states, such as the intervalley coherent Kekulé spiral state[50], can be considered but do not change the light–heavy dichotomy in the dispersion of the symmetry-broken states. At $\nu = 0$, the bands near E_F consist of light excitations for both holes and electrons. As the charge ±1 excitations are symmetric around E_F, the Seebeck coefficient (Fig. 3e) exhibits a conventional antisymmetric line shape, consistent with our observations for MATBG near CNP (Fig. 1e).

The interacting THF band structures for the symmetry-broken ground states at non-zero integer ν (shown in Fig. 3c,d) exhibit a marked asymmetry of the charge ±1 excitations. We found that the low-energy hole-like excitations correspond to localized f states, while itinerant c electrons form the bands just above E_F. The strong interactions between f states lead to a reduced τ for the heavy carriers near E_F. Indeed, we found that the symmetry-broken correlated insulators at positive integer fillings replicate the light–heavy scenario sketched in Fig. 2d, as the weakly dispersive hole band features states with reduced carrier lifetimes.

We then computed the Seebeck coefficient for the symmetry-broken states at non-zero integer fillings (Fig. 3c,d). The hole-like contributions to thermoelectricity are quenched due to the reduction of τ for the localized f states, resulting in a fully negative Seebeck coefficient across the interaction-driven gaps near $\nu = 1,2$. These findings align well with our experimental observations (Fig. 2a). Notably, for $\nu = 1,2$, the negative peak of S is shifted towards the CNP in the theoretical computations. This effect, also present in the experimental data, arises from the highly broadened spectral weight of the f-electron bands below E_F (ref. 33). Detailed THF band structures and Seebeck coefficients for different ground states, fillings and temperatures are presented in ref. 36.

Overall, the light–heavy structure of the symmetry-broken correlated states within the THF model provides a natural explanation for the observed PTE response at low temperatures. The crucial role of the finite carrier lifetimes of the f states is emphasized in the observation of a negative, sign-preserving Seebeck coefficient. From the measured response and the estimated ΔT_e (Supplementary Section IV), we obtained $S \approx 50\text{–}150$ μV K^{-1} for $T_L = 10$ K across the conduction flat band, in good agreement with theoretical computations[36] and previous reports[26–28]. We note that, while the Seebeck coefficient is typically small in semimetals, due to e–h compensation, the asymmetry in dispersion and lifetime in the correlated states of MATBG leads to a large Seebeck coefficient.

We now focus on thermoelectric transport at higher lattice temperatures. As the temperature rises, the symmetry-broken ground states disappear and MATBG transitions into a symmetry-preserving unordered state[47,51], with Hubbard bands observed in scanning tunnelling microscopy experiments[52,53]. Theoretical calculations estimate the critical temperature for this symmetric state to be around 10–20 K (ref. 47). The PTE response at $T_L = 30$ K and 50 K for an absorbed optical power $P_{abs} = 5.47$ μW is illustrated in Fig. 4a. Unlike the low-temperature behaviour, we observe hole-like thermoelectricity with $S > 0$ for $0 < \nu_1 < 3$, which we attribute to the activation of carriers in higher energy bands. The overall trend of the signal resembles the thermoelectric response in the non-interacting limit (grey trace in Fig. 4a). However, the distinct gap-like oscillations around each integer ν_1 (Fig. 4b) indicate the persistence of electron correlations in the high-temperature, symmetric state.

To model the high-temperature thermoelectric transport, we used the THF model with identical parameters to the low-temperature case. However, we examined symmetric solutions, in which none of the model's symmetries are spontaneously broken[36,51,54]. The computed symmetric Seebeck coefficient S_{Sym} is illustrated in Fig. 4c for $T_L = 15$ K, and shows marked oscillations at integer ν along with a positive (hole-like) offset, similar to the non-interacting scenario[36]. The oscillations arise from gap openings through interactions between the localized f states. Overall, the THF model qualitatively reproduces the Seebeck effect at high temperatures under the assumption that the solution must preserve symmetry. The temperature mismatch between the theory and experiment stems from less precise modelling of the non-interacting dispersion, which is susceptible to extrinsic effects such as strain or lattice relaxation.

The PTE response at elevated temperatures highlights the presence of electron correlations beyond the ordering temperatures of the symmetry-broken ground states. The qualitative match with the Seebeck coefficient for the symmetric solution of the THF model provides further support for heavy fermion physics in MATBG. These findings also emphasize that electron interactions can induce gap openings in the electronic spectrum of the flat band even when all system symmetries are preserved.

While the band asymmetry of the correlated ground states has been predicted in other theoretical frameworks[29–33], heavy fermion mapping of MATBG[35] offers two distinct advantages. First, it enables computations beyond the Hartree–Fock level, allowing us to self-consistently obtain the band and state-resolved carrier lifetime,

which is central to the observed low-temperature behaviour. Second, it provides an intuitive picture of the contrasting ground states observed in the MATBG flat bands based on the coexistence of distinct carrier types with different masses and scattering rates.

Future studies of the thermoelectricity of MATBG flat bands could investigate the Nernst effect[21,55] or locally map thermoelectric transport[56]. The role of phonon drag contributions, particularly for Joule heating schemes, remains an open question due to the limited experimental insight into the phonon spectrum of MATBG and its coupling to electronic transport[57,58]. The signatures of coexisting light and heavy electrons reported here also motivate the investigation of Kondo physics in van der Waals heterostructures[59–62].

In terms of applications, the large measured PTE response (and predicted Seebeck coefficient) suggest the potential for applications of MATBG as a thermoelectric material; for example, in active thermoelectric cooling at cryogenic temperatures[55,63]. Correlated materials have been proposed before as excellent candidates for thermoelectric materials[22,64]. Future MATBG devices based on the PTE effect could leverage broadband absorption[65], efficient carrier heating[42,43] and ultrafast thermal relaxation[57].

Online content

Any methods, additional references, Nature Portfolio reporting summaries, source data, extended data, supplementary information, acknowledgements, peer review information; details of author contributions and competing interests; and statements of data and code availability are available at https://doi.org/10.1038/s41567-025-02912-x.

References

1. Bistritzer, R. & MacDonald, A. H. Moiré bands in twisted double-layer graphene. *Proc. Natl Acad. Sci. USA* **108**, 12233–12237 (2011).
2. Balents, L., Dean, C. R., Efetov, D. K. & Young, A. F. Superconductivity and strong correlations in moir, flat bands. *Nat. Phys.* **7**, 725–733 (2020).
3. Cao, Y. et al. Unconventional superconductivity in magic-angle graphene superlattices. *Nature* **556**, 43–50 (2018).
4. Lu, X. et al. Superconductors, orbital magnets and correlated states in magic-angle bilayer graphene. *Nature* **574**, 653–657 (2019).
5. Yankowitz, M. et al. Tuning superconductivity in twisted bilayer graphene. *Science* **363**, 1059–1064 (2019).
6. Cao, Y. et al. Correlated insulator behaviour at half-filling in magic-angle graphene superlattices. *Nature* **556**, 80–84 (2018).
7. Serlin, M. et al. Intrinsic quantized anomalous Hall effect in a moiré heterostructure. *Science* **367**, 900–903 (2020).
8. Choi, Y. et al. Correlation-driven topological phases in magic-angle twisted bilayer graphene. *Nature* **589**, 536–541 (2021).
9. Das, I. et al. Symmetry-broken Chern insulators and Rashba-like Landau-level crossings in magic-angle bilayer graphene. *Nat. Phys.* **17**, 710–714 (2021).
10. Wu, S., Zhang, Z., Watanabe, K., Taniguchi, T. & Andrei, E. Y. Chern insulators, van Hove singularities and topological flat bands in magic-angle twisted bilayer graphene. *Nat. Mater.* **20**, 488–494 (2021).
11. Zondiner, U. et al. Cascade of phase transitions and Dirac revivals in magic-angle graphene. *Nature* **582**, 203–208 (2020).
12. Wong, D. et al. Cascade of electronic transitions in magic-angle twisted bilayer graphene. *Nature* **582**, 198–202 (2020).
13. Park, J. M., Cao, Y., Watanabe, K., Taniguchi, T. & Jarillo-Herrero, P. Flavour Hund's coupling, Chern gaps and charge diffusivity in moiré graphene. *Nature* **592**, 43–48 (2021).
14. Saito, Y. et al. Isospin Pomeranchuk effect in twisted bilayer graphene. *Nature* **592**, 220–224 (2021).
15. Rozen, A. et al. Entropic evidence for a Pomeranchuk effect in magic-angle graphene. *Nature* **592**, 214–219 (2021).
16. Cutler, M. & Mott, N. F. Observation of Anderson localization in an electron gas. *Phys. Rev.* **181**, 1336–1340 (1969).
17. Chang, J. et al. Nernst and Seebeck coefficients of the cuprate superconductor $YBa_2Cu_3O_{6.67}$: a study of Fermi surface reconstruction. *Phys. Rev. Lett.* **104**, 057005 (2010).
18. Laliberté, F. et al. Fermi-surface reconstruction by stripe order in cuprate superconductors. *Nat. Commun.* **2**, 432 (2011).
19. Gourgout, A. et al. Seebeck coefficient in a cuprate superconductor: particle-hole asymmetry in the strange metal phase and Fermi surface transformation in the pseudogap phase. *Phys. Rev. X* **12**, 011037 (2022).
20. Ijiri, Y. & DiSalvo, F. J. Thermoelectric properties of $R_xCe_{1-x}Pd_3$ (R=Y, $La_{0.5}Y_{0.5}$, Nd). *Phys. Rev. B* **55**, 1283–1287 (1996).
21. Sun, P. & Steglich, F. Nernst effect: evidence of local Kondo scattering in heavy fermions. *Phys. Rev. Lett.* **110**, 216408 (2013).
22. Tomczak, J. M. Thermoelectricity in correlated narrow-gap semiconductors. *J. Phys. Condens. Matter* **30**, 183001 (2018).
23. Xie, H. et al. Anomalously large Seebeck coefficient of $CuFeS_2$ derives from large asymmetry in the energy dependence of carrier relaxation time. *Chem. Mater.* **32**, 2639–2646 (2020).
24. Sun, P. et al. Large Seebeck effect by charge-mobility engineering. *Nat. Commun.* **6**, 7475 (2015).
25. Jie, Q. et al. Electronic thermoelectric power factor and metal-insulator transition in $FeSb_2$. *Phys. Rev. B* **86**, 115121 (2012).
26. Paul, A. K. et al. Interaction-driven giant thermopower in magic-angle twisted bilayer graphene. *Nat. Phys.* **18**, 691–698 (2022).
27. Ghawri, B. et al. Breakdown of semiclassical description of thermoelectricity in near-magic angle twisted bilayer graphene. *Nat. Commun.* **13**, 1522 (2022).
28. Bhowmik, S. et al. Broken-symmetry states at half-integer band fillings in twisted bilayer graphene. *Nat. Phys.* **18**, 639–643 (2022).
29. Vafek, O. & Kang, J. Renormalization group study of hidden symmetry in twisted bilayer graphene with Coulomb interactions. *Phys. Rev. Lett.* **125**, 257602 (2020).
30. Bernevig, B. A. et al. Twisted bilayer graphene. V. Exact analytic many-body excitations in Coulomb Hamiltonians: charge gap, Goldstone modes, and absence of Cooper pairing. *Phys. Rev. B* **103**, 205415 (2021).
31. Kang, J., Bernevig, B. A. & Vafek, O. Cascades between light and heavy fermions in the normal state of magic-angle twisted bilayer graphene. *Phys. Rev. Lett.* **127**, 1–18 (2021).
32. Kumar, A., Xie, M. & MacDonald, A. H. Lattice collective modes from a continuum model of magic-angle twisted bilayer graphene. *Phys. Rev. B* **104**, 035119 (2021).
33. Xie, F., Kang, J., Bernevig, B. A., Vafek, O. & Regnault, N. Phase diagram of twisted bilayer graphene at filling factor $\nu = \pm 3$. *Phys. Rev. B* **107**, 075156 (2023).
34. Georges, A. & Mravlje, J. Skewed non-Fermi liquids and the Seebeck effect. *Phys. Rev. Res.* **3**, 043132 (2021).
35. Song, Z. D. & Bernevig, B. A. Magic-angle twisted bilayer graphene as a topological heavy fermion problem. *Phys. Rev. Lett.* **129**, 047601 (2022).
36. Călugăru, D. The thermoelectric effect in twisted bilayer graphene in the heavy fermion picture. Preprint at https://arxiv.org/abs/2402.14057 (2024).
37. Calderón, M. J. & Bascones, E. Interactions in the 8-orbital model for twisted bilayer graphene. *Phys. Rev. B* **102**, 155149 (2020).
38. Gabor, N. M. et al. Hot carrier–assisted intrinsic photoresponse in graphene. *Science* **334**, 648–652 (2011).
39. Song, J. C. W., Rudner, M. S., Marcus, C. M. & Levitov, L. S. Hot carrier transport and photocurrent response in graphene. *Nano Lett.* **11**, 4688–4692 (2011).
40. Xu, X., Gabor, N. M., Alden, J. S., Van Der Zande, A. M. & McEuen, P. L. Photo-thermoelectric effect at a graphene interface junction. *Nano Lett.* **10**, 562–566 (2010).

41. Lemme, M. C. et al. Gate-activated photoresponse in a graphene p–n junction. *Nano Lett.* **11**, 4134–4137 (2011).
42. Tielrooij, K. J. et al. Photoexcitation cascade and multiple hot-carrier generation in graphene. *Nat. Phys.* **9**, 248–252 (2013).
43. Tielrooij, K. J. et al. Generation of photovoltage in graphene on a femtosecond timescale through efficient carrier heating. *Nat. Nanotechnol.* **10**, 437–443 (2015).
44. Massicotte, M., Soavi, G., Principi, A. & Tielrooij, K.-J. Hot carriers in graphene – fundamentals and applications. *Nanoscale* **13**, 8376–8411 (2021).
45. Di Battista, G. et al. Revealing the thermal properties of superconducting magic-angle twisted bilayer graphene. *Nano Lett.* **22**, 6465–6470 (2022).
46. Hubmann, S. et al. Infrared photoresistance as a sensitive probe of electronic transport in twisted bilayer graphene. *2D Mater.* **10**, 015005 (2023).
47. Rai, G. et al. Dynamical correlations and order in magic-angle twisted bilayer graphene. *Phys. Rev. X* **14**, 031045 (2024).
48. Zlatić, V., Monnier, R., Freericks, J. K. & Becker, K. W. Relationship between the thermopower and entropy of strongly correlated electron systems. *Phys. Rev. B* **76**, 085122 (2007).
49. Bultinck, N. et al. Ground state and hidden symmetry of magic-angle graphene at even integer filling. *Phys. Rev. X* **10**, 031034 (2020).
50. Kwan, Y. H. et al. Kekulé spiral order at all nonzero integer fillings in twisted bilayer graphene. *Phys. Rev. X* **11**, 041063 (2021).
51. Datta, A., Calderón, M. J., Camjayi, A. & Bascones, E. Heavy quasiparticles and cascades without symmetry breaking in twisted bilayer graphene. *Nat. Commun.* **14**, 5036 (2023).
52. Xie, Y. et al. Spectroscopic signatures of many-body correlations in magic-angle twisted bilayer graphene. *Nature* **572**, 101–105 (2019).
53. Kerelsky, A. et al. Maximized electron interactions at the magic angle in twisted bilayer graphene. *Nature* **572**, 95–100 (2019).
54. Wagner, G., Kwan, Y. H., Bultinck, N., Simon, S. H. & Parameswaran, S. A. Global phase diagram of the normal state of twisted bilayer graphene. *Phys. Rev. Lett.* **128**, 156401 (2022).
55. Pasquale, G. et al. Electrically tunable giant Nernst effect in two-dimensional van der Waals heterostructures. *Nat. Nanotechnol.* https://doi.org/10.1038/s41565-024-01717-y (2024).
56. Völkl, T. et al. Demonstration and imaging of cryogenic magneto-thermoelectric cooling in a van der Waals semimetal. *Nat. Phys.* https://doi.org/10.1038/s41567-024-02417-z (2024).
57. Mehew, J. D. et al. Ultrafast Umklapp-assisted electron-phonon cooling in magic-angle twisted bilayer graphene. *Sci. Adv.* **10**, eadj1361 (2024).
58. Birkeck, J. et al. Measuring phonon dispersion and electron-phason coupling in twisted bilayer graphene with a cryogenic quantum twisting microscope. *Nature* https://doi.org/10.1038/s41586-025-08881-8 (2025).
59. Ramires, A. & Lado, J. L. Emulating heavy fermions in twisted trilayer graphene. *Phys. Rev. Lett.* **127**, 026401 (2021).
60. Vaňo, V. et al. Artificial heavy fermions in a van der Waals heterostructure. *Nature* **599**, 582–586 (2021).
61. Zhao, W. et al. Gate-tunable heavy fermions in a moiré Kondo lattice. *Nature* **616**, 61–65 (2023).
62. Posey, V. A. et al. Two-dimensional heavy fermions in the van der Waals metal CeSiI. *Nature* **625**, 483–488 (2024).
63. Duan, J. et al. High thermoelectricpower factor in graphene/hBN devices. *Proc. Natl Acad. Sci. USA* **113**, 14272–14276 (2016).
64. Urban, J. J., Menon, A. K., Tian, Z., Jain, A. & Hippalgaonkar, K. New horizons in thermoelectric materials: correlated electrons, organic transport, machine learning, and more. *J. Appl. Phys.* **125**, 180902 (2019).
65. Nair, R. R. et al. Fine structure constant defines visual transparency of graphene. *Science* **320**, 1308–1308 (2008).

Methods

Device fabrication

The MATBG devices were fabricated using a cut-and-stack technique. All flakes were first exfoliated on a Si/SiO_2 (285 nm) substrate and later picked up using a polycarbonate (PC)/polydimethylsiloxane (PDMS) stamp. All of the layers were picked up at a temperature of $T \approx 100$ °C. We used an atomic force microscope tip to cut the graphene to avoid strain during the pick-up process. The PC/PDMS stamp first picked up the top graphite layer, the top hBN and the first graphene layer. Before picking up the second graphene layer, we rotated the stage by an angle of $\theta = 1.1°$. Finally, the stamp picked up the bottom hBN and bottom graphite gates. We dropped the finalized stack onto a Si/SiO_2 substrate by melting the PC at $T \approx 180$ °C. The resulting stack was etched into a Hall bar using a CHF_3/O_2 plasma and one-dimensional contacts were formed by evaporating Cr (5 nm)/Au (50 nm) (Supplementary Fig. 1b). We etched a narrow channel of width $d \approx 150$ nm in the top gate using an O_2 plasma. Before etching the top gate, the device was characterized in transport using a four-probe configuration at $T_L = 35$ mK to identify the pair of contacts closest to the magic angle of $\theta = 1.1°$. The junction was made between this pair of contacts.

Transport measurements

Transport studies for the characterization of the two samples were carried out in a dilution refrigerator (BlueFors SD250) with a base temperature of 20 mK and a VTI cryostat (ICEOxford) with a base temperature of 1.55 K. Further transport measurements were performed in situ in the optical cryostat (Attodry 800, base temperature 6 K) used for the optoelectronic measurements. All transport measurements were performed using a standard low-frequency lock-in technique (Stanford Research SR860 amplifiers) with frequency $f = 17.177$ Hz.

Optoelectronic measurements

We studied the optoelectronic response of the MATBG p–n junctions using standard d.c. and low-frequency a.c. transport measurements combined with scanning laser microscopy. All optoelectronic measurements were performed in an Attodry 800 cryostat with free-space optical access. Further information on the optoelectronic set-up is provided in the Supplementary Information.

Data availability

Source data are provided with this paper. All other datasets that support the plots within this publication are available from the corresponding author upon reasonable request.

Acknowledgements

We thank N. Regnault, A. Jaoui, E.Y. Andrei, S. Buhler-Paschen, F. Koppens, L. Lin, A. Georges, A. Millis and G. Sangiovanni for useful discussions. D.C. acknowledges the hospitality of the Donostia International Physics Center, at which this work was carried out. B.A.B. was supported by DOE grant number DE-SC0016239. D.C. was supported by the European Research Council (ERC) under the European Union's Horizon 2020 research and innovation programme (grant agreement number 101020833) and by Simons Investigator grant number 404513, the Gordon and Betty Moore Foundation through grant number GBMF8685 towards the Princeton theory programme, the Gordon and Betty Moore Foundation's EPiQS Initiative (grant number GBMF11070), the Office of Naval Research (ONR grant number N00014-20-1-2303), the Global Collaborative Network Grant at Princeton University, BSF Israel US foundation number 2018226 and NSF-MERSEC (grant number MERSEC DMR 2011750). D.C. also gratefully acknowledges the support provided by the Leverhulme Trust. H.H. was supported by the European Research Council (ERC) under the European Union's Horizon 2020 research and innovation programme (grant agreement number 101020833) and the Schmidt Fund Grant. P.S. acknowledges support from the Alexander von-Humboldt Foundation and the German Federal Ministry for Education and Research through the Feodor-Lynen programme. J.D.-M. acknowledges support from the INPhINIT 'la Caixa' Foundation (ID 100010434) fellowship programme (grant number LCF/BQ/DI19/11730021). D.K.E. acknowledges funding from the European Research Council (ERC) under the European Union's Horizon 2020 research and innovation programme (grant agreement number 852927) and the German Research Foundation (DFG) under the priority programme SPP2244 (project number 535146365). K.W. and T.T. acknowledge support from the Elemental Strategy Initiative conducted by the MEXT, Japan (grant number JPMXP0112101001), and JSPS KAKENHI (grant numbers 19H05790, 20H00354 and 21H05233).

Author contributions

R.L.M., P.S. and D.K.E conceived and designed the experiments. R.L.M., P.S., J.D.-M. and A.D.-C. performed the transport measurements. R.L.M. and P.S. performed the optoelectronic measurements. J.D.-M and A.D.-C. fabricated the samples. R.L.M. and P.S. performed the data analysis. D.C., H.H. and B.A.B. performed the theoretical modelling. T.T. and K.W. provided materials. R.L.M. and D.K.E. wrote the paper with input from D.C., H.H. and B.A.B.

Funding

Open access funding provided by Ludwig-Maximilians-Universität München.

Competing interests

The authors declare no competing interests.

Additional information

Supplementary information The online version contains supplementary material available at https://doi.org/10.1038/s41567-025-02912-x.

Correspondence and requests for materials should be addressed to Dmitri K. Efetov.

Peer review information *Nature Physics* thanks Nathaniel Gabor, Mona Zebarjadi and the other, anonymous, reviewer(s) for their contribution to the peer review of this work.